Swansea University
Prifysgol Abertawe

Cronfa
Setting Research Free

Cronfa - Swansea University Open Access Repository

This is an author produced version of a paper published in:
Results in Physics

Cronfa URL for this paper:
http://cronfa.swan.ac.uk/Record/cronfa44994

Paper:
Litvin, I., Alkoby, Y., Godsi, O., Alexandrowicz, G. & Maniv, T. (2019). Parallel and anti-parallel echoes in beam spin echo experiments. *Results in Physics, 12*, 381-391.
http://dx.doi.org/10.1016/j.rinp.2018.09.032

Released under the terms of a Creative Commons Attribution 4.0 International License (CC-BY).

This item is brought to you by Swansea University. Any person downloading material is agreeing to abide by the terms of the repository licence. Copies of full text items may be used or reproduced in any format or medium, without prior permission for personal research or study, educational or non-commercial purposes only. The copyright for any work remains with the original author unless otherwise specified. The full-text must not be sold in any format or medium without the formal permission of the copyright holder.

Permission for multiple reproductions should be obtained from the original author.

Authors are personally responsible for adhering to copyright and publisher restrictions when uploading content to the repository.

http://www.swansea.ac.uk/library/researchsupport/ris-support/

Results in Physics 12 (2019) 381–391

Contents lists available at ScienceDirect

Results in Physics

journal homepage: www.elsevier.com/locate/rinp

Parallel and anti-parallel echoes in beam spin echo experiments

I. Litvin[a], Y. Alkoby[a], O. Godsi[a], G. Alexandrowicz[a,b,*], T. Maniv[a,*]

[a] Schulich Faculty of Chemistry, Technion – Israel Institute of Technology, Technion City, Haifa 32000, Israel
[b] Department of Chemistry, Swansea University, Singleton Park, Swansea SA2 8PP, United Kingdom

ABSTRACT

The refocusing of velocity-dependent spin-phase is the basic phenomenon behind helium and neutron spin echo beam experiments. In this paper we present quantum and classical descriptions of the spin echo phenomenon and show that non-adiabatic transitions, such as those which take place during rotation of the magnetic field axis between the two arms of a helium spin echo setup, lead to echo conditions without reversing the magnetic field orientation between the two arms. The usual spin echo conditions, created by reversing the magnetic field orientation, do not require such non-adiabatic transitions. These two echo conditions are termed parallel and anti-parallel spin echoes, respectively. We derive the dependence of the relative intensity of the two echoes on the scattering geometry of the setup and show experimental results which verify the co-existence of the two echo conditions, the theoretically derived expressions for their relative intensity and the effect of an additional spin rotator coil introduced within the non-adiabatic transition region.

Introduction

Neutron spin echo (NSE) and helium spin echo (HSE) are two beam techniques with exceptionally high energy resolution which have revolutionized the ability to study atomic scale bulk and surface dynamics [1,2]. While studying atomic scale dynamics, is by far the most common application of HSE and NSE, these setups can also be used to perform various other unique experiments, such as measuring the interaction potentials of atoms and surfaces, high resolution measurements of phonon spectra, controlling the rotational state of a molecule, studying vibrational lifetime of adsorbates and even performing subtle measurements of gravitation induced quantum interference [3–8].

While HSE and NSE are usually used to study different type of samples (mainly surface versus bulk samples), both experimental techniques use spin 1/2 particles (helium-3/neutrons) and hence share many similarities in the basic description of the spin dynamics through the magnetic fields of the apparatus. In fact, for materials with extremely high surface area, both techniques can be applied providing complementary information [9]. One common aspect of both beam techniques is the spin echo signal. Similarly to the well-known spin echo signal in nuclear magnetic resonance[10], the spin echo signal in NSE and HSE experiments results from the refocusing of the macroscopic magnetic moment. This signal can be obtained with a particular combination of magnetic fields, often termed the spin echo condition.

Several different theoretical descriptions have been developed over the years to explain the basic spin echo experiment using classical and quantum derivations (e.g. [1,11]). Since the invention of the basic NSE experiment, further variants have been developed which involve magnetic manipulation using oscillating transverse and longtitudal RF fields (see for example [12–14]). For simplicity, we will limit the description of the spin dynamics to the basic setups shown schematically in Fig. 1, which use two DC longitudinal magnetic fields for spin manipulation. The schematic setup in the upper drawing has an acute total scattering angle, Θ_{tot}, which is typical for HSE experiments, whereas the lower one has an obtuse total scattering angle, which is typical in many NSE experiments. In both cases the beam particles are produced at the source and polarized along the Z axis. They enter a solenoid coil which produces a longitudinal magnetic field ($\vec{B}_1$) aligned along the X axis. After exiting this field they pass through an optional spin rotator coil, which can be used to produce a magnetic field along the Y axis, and then scatter from the surface (HSE) or bulk (NSE). For simplicity we will restrict ourselves to elastic scattering, i.e. the velocity of the particles does not change during the scattering event. The scattered beam passes through a second solenoid coil producing a magnetic field ($\vec{B}_2$) and then enters a spin analyzer which transmits the particles toward the particle detector depending on their Z' spin polarization.

The following heuristic explanation is commonly used to introduce NSE and HSE experiments and is based on the following simple classical arguments. Applying a constant magnetic field to a magnetic moment which is initially aligned at an angle to that field, will lead to the precession of the moment within the plane perpendicular to the field. The frequency of the precession is proportional to the magnetic field magnitude and is known as the Larmor frequency, $\omega_L = \gamma B$, where $\gamma$is the gyromagnetic ratio of the beam particles. Initially all the beam particles are aligned along the same axis, however, particles with different velocities will spend a different period of time within the first

* Corresponding authors.
E-mail addresses: ga232@technion.ac.il (G. Alexandrowicz), maniv@technion.ac.il (T. Maniv).

https://doi.org/10.1016/j.rinp.2018.09.032
Received 12 July 2018; Received in revised form 21 August 2018; Accepted 15 September 2018
Available online 21 September 2018
2211-3797/ © 2018 The Authors. Published by Elsevier B.V. This is an open access article under the CC BY license (http://creativecommons.org/licenses/BY/4.0/).

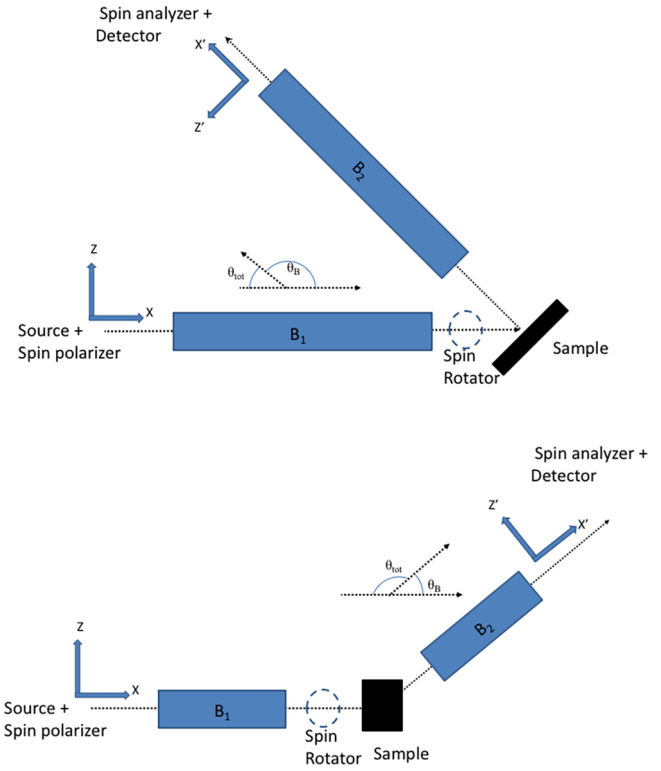

Fig. 1. Schematic of two spin echo setups with different configurations of longitudinal magnetic fields. The upper plot shows a total scattering angle of 45° which is often used in HSE experiments. The lower plot shows a configuration with an obtuse total scattering angle which is more typical in NSE experiments.

magnetic field B_1 . Consequently, if the field is strong enough, the different particles will accumulate different spin phases while moving through the field, the orientation of the magnetic moments will be significantly spread out and the average macroscopic magnetic moment (magnetization) of the beam will decay to zero before it reaches the sample. However, similarly to inhomogeneous broadening in NMR [10], this effect can be reversed and the macroscopic magnetization can be recovered if the second magnetic field, B_2, produces a net phase change which exactly cancels out the spread of spin phases which existed before the particles entered the second field.

HSE and NSE setups can have different geometries, consequently the relative polarity of the two fields needed to obtain a spin echo, which is a key point of this study, is a bit tricky to define unambiguously. Since in this paper we will restrict ourselves to longitudinal B_1 and B_2 fields, we will use the following definition scheme: We will assume that $\vec{B_1}$ is aligned along the X axis which marks the beam propagation axis before reaching the sample (see Fig. 1). We will denote the configuration where $\vec{B_2}$ is aligned parallel to the scattered beam propagation axis (X') as the parallel echo configuration as opposed to a reversed $\vec{B_2}$ polarity which we will call the anti-parallel echo configuration [15].

An important difference in the spin dynamics between HSE and NSE setups is the magnetic field at the sample position. In the traditional NSE experiment the fringe fields of B_1 and B_2 overlap at the sample position, and the spin undergoes an adiabatic transition, i.e. the plane within which the spins percess rotates continuously as the particles move from the B_1 magnetic field region (where the precession takes place in YZ plane) into the B_2 region (where the precession takes place in the YZ' plane). Here we use the terms adiabatic/non-adiabatic in the classical sense often used by the NSE and NMR communities[16], namely, adiabatic/non-adiabatic transitions correspond to field geometries where the rate of change in the magnetic field direction is smaller/larger than the Larmor frequency at the transition region.

The first HSE setup built in Heidelberg [17] followed the NSE design and used an adiabatic transition in between B_1 and B_2 . In contrast, the HSE setups built later in Cambridge and the Technion[18,19], included a magnetically shielded scattering chamber and were designed to fully isolate the B_1 and B_2 fields. The fact that the sample is located in a zero-field region ($\omega_L \rightarrow 0$), results in a non-adiabatic (sudden) spin transition into B_2.

In NSE setups, where the B_1 and B_2 fields are in the parallel configuration defined above, there are two requirements to obtain a cancellation of the spin phase accumulated in the two fields (1) The fields have to be equal $B_1 = B_2$ and (2) An additional 180° rotation is applied in the region between the two fields to flip the phase accumulated in B_1. For HSE setups with a zero field at the sample location, the non-adiabatic transition leads to a more complex scenario. The spin echo condition can be tuned experimentally by scanning the amplitude of one of the two fields (B_1 or B_2) while keeping the other fixed. Traditionally, this is done at a set of discreet magnetic field values, although continuous modulation of one of the fields has also been demonstrated recently [20].

In this paper we reexamine the fundamental mechanism controlling the formation of spin echo in the presence of such non-adiabatic transitions. Using a quantum mechanical description of spin echo beam experiments, we reveal an alternative channel of spin echo, so far unnoticed in the current literature, which is exclusively associated with the non-adiabatic nature of the spin dynamics in the region between the two fields. We provide a rigorous derivation of the spin evolution through a simplified HSE setup and show theoretically and experimentally that the combination of a non-adiabatic transition with realistic conditions for the total scattering angle ($0° > \Theta_{tot} > 180°$) leads to spin echo conditions at $B_1 = B_2$, in addition to the commonly used conditions at $B_1 = -B_2$. The two echoes, termed here parallel and anti-parallel spin echoes, respectively, can be measured on the same setup and have relative intensities that depend on Θ_{tot} and can be continuously converted between the two using a rotator coil. Finally, we show that the relative intensity between the parallel and anti-parallel echoes provides a way of assessing the magnetic profile the beam particles propagate through.

Quantum description of the echo signal in a beam of spin 1/2 particles

In this section we use a mixed quantum–classical approach to derive analytical expressions showing the existence and relative intensities of the parallel and anti-parallel spin echoes. A completely classical approach, described in the next section, can also be used to reach the same conclusions. However, employing a quantum approach becomes mandatory if one wishes to later extend this concept to molecular beams with nuclear spins coupled to rotational magnetic moments, a new exciting option which has been recently demonstrated experimentally [6]. Keeping these developments in mind, our derivation here, which is made specifically for a beam of spin 1/2 particles, is written in such general terms that is straightforwardly extendable to higher spin systems.

In our mixed quantum-classical approach, the center of mass motion of the particle is treated classically and the internal (nuclear-spin) degrees of freedom are treated quantum mechanically. We also assume that the particle velocity remains constant along the entire classical trajectory. In this approach, the internal nuclear state vector at a given time in each arm along its classical path, is expanded in the complete orthonormal set of eigenvectors of the spin Hamiltonian under a magnetic field oriented along the beam axis (see Fig.1 upper plot).

The magnetic field within a given field zone (e.g., as inside one of the solenoids) is approximately uniform on the relevant length scale involved, and the corresponding eigenstates problem is solved by replacing the transition region between neighboring field-zones with a

single interface, then imposing continuity boundary conditions on the state vector at the interface. We will show in Appendix A that the picture of the nuclear spin/magnetic-moment, moving along a single classical trajectory, as described above, is to leading order in the small magnetic-to-kinetic energy ratio, fully consistent with the Stern-Gerlach velocity splitting generated by the field gradient at the interface. It should be noted, however, that in this model the spin dynamics follows adiabatically the particle center-of-mass motion in each arm whereas non-adiabatic spin dynamics takes place only in the transition region due to the rotation of the magnetic field axis between the two field zones (see below for more details).

Since the initial magnetic lens polarizes the particle along an axis (Z) perpendicular to the beam (see Fig. 1), the eigenvectors in the first arm are obtained from the eigenvectors of the initial spin Hamiltonian by the unitary transformation, associated with the rotation of the magnetic field direction from the Z-axis to the beam (X) axis. Similarly, since a particle entering the detector is probed there through its magnetic polarization along an axis (Z') perpendicular to the direction (X') of the second arm, the eigenvectors in the second arm are obtained from the eigenvectors in the detecting region by the transformation associated with the $Z' \rightarrow X'$ rotation.

Starting with an initial state vector $|\Psi(0)\rangle$ of the particle, prepared at the beam source as a pure quantum state with spin projection along the Z-axis, its state vector, $|\Psi_1(t)\rangle$ in the first solenoid ($0 \leqslant t < \tau_1$, $\vec{B_1} = B_1\widehat{X}$) is calculated by expanding in the eigenvectors, $|x_1^{(1)}\rangle$, $|x_2^{(1)}\rangle$, ..., of the spin Hamiltonian under a magnetic field oriented along the beam propagation direction, $\widehat{X}$, with the field intensity, B_1:

$$|\Psi_1(t)\rangle = \sum_n A_n^{(1)} e^{-i\omega_n(B_1)t}\ |x_n^{(1)}\rangle \tag{1}$$

Here $\hbar\omega_n(B_1)$ ($n = 1, 2$ for the case of spin $\frac{1}{2}$), are the eigenvalues of the spin Hamiltonian for magnetic field intensity B_1, and $|x_n^{(1)}\rangle$ are obtained from the eigenvectors, $|z_n^{(1)}\rangle$, of the spin Hamiltonian in a magnetic field $B_1\widehat{Z}$, by applying the unitary transformation $U(\pi/2)^\dagger$, corresponding to a $\pi/2$ rotation of the reference of frames around its Y-axis, i.e.:

$$|x_n^{(1)}\rangle = U(\pi/2)^\dagger |z_n^{(1)}\rangle \tag{2}$$

Thus, the coefficients $A_n^{(1)}$, determining the state vector in the first solenoid, are obtained by applying the initial condition at $t = 0$, i.e.: $|\Psi_1(t=0)\rangle = U(\pi/2)^\dagger \sum_n A_n^{(1)}\ |z_n^{(1)}\rangle = |\Psi(0)\rangle$, which yields for the coefficients:

$$A_n^{(1)} = \langle z_n^{(1)}|U(\pi/2)|\Psi(0)\rangle \tag{3}$$

Defining a diagonal dynamical matrix $\Lambda_{n,n}^{(1)}(t) \equiv e^{-i\omega_n(B_1)t}$, and exploiting the solution Eq. (3), we can then write an explicit expression for $|\Psi_1(t)\rangle$ in terms of the initial state vector $|\Psi(0)\rangle$ in the form:

$$|\Psi_1(t)\rangle = U(\pi/2)^\dagger \left[\sum_n |z_n^{(1)}\rangle \Lambda_{n,n}^{(1)}(t) \langle z_n^{(1)}|\right] U(\pi/2)|\Psi(0)\rangle \tag{4}$$

In the scattering region, $\tau_1 \leqslant t < \tau_2$, we will assume, for simplicity, that the spin rotator coil is de-energized and that within this region the particle is moving in a field free region, $B = 0$. The particle enters the region at time τ_1 (at the end of the first solenoid), then scatters from the sample surface into the second arm at a later time $\tau_s = \tau_1 + \tau_0$, where its free motion continues up to the entrance to the second solenoid at time $\tau_2 = \tau_s + \tau_0$. The state vector $|\Psi_2(t)\rangle$ in the second solenoid ($\tau_2 \leqslant t < \tau_3$, $\vec{B_2} = B_2\widehat{X}'$) is obtained by expanding in the eigenvectors, $|x_1'^{(2)}\rangle$, $|x_2'^{(2)}\rangle$, ..., of the spin Hamiltonian under a magnetic field oriented along the beam propagation axis, $\widehat{X}'$, with the field intensity, B_2:

$$|\Psi_2(t)\rangle = \sum_n A_n^{(2)} e^{-i\omega_n(B_2)t}\ |x_n'^{(2)}\rangle,\ \tau_2 \leqslant t < \tau_3 \tag{5}$$

Here $\hbar\omega_n(B_2)$, are the eigenvalues of the spin Hamiltonian for magnetic field intensity B_2, and $|x_n'^{(2)}\rangle$ are obtained from the eigenvectors, $|z_n'^{(2)}\rangle$, of the Hamiltonian in the same magnetic field intensity (B_2), but oriented along the magnetic field in the detection region, by applying the unitary transformation $U(\pi/2)^\dagger$, corresponding to a $\pi/2$ rotation of the reference of frames around the Y-axis (see Fig. 1), i.e.:

$$|x_n'^{(2)}\rangle = U(\pi/2)^\dagger |z_n'^{(2)}\rangle \tag{6}$$

To illustrate how the concept of spin echo is built into our system let us consider a simplified model in which the two solenoids are directly connected at $\tau_1 = \tau_s = \tau_2$, where the beam center of mass undergoes reflection, but without changing its internal (magnetic) state. Assigning a length L to each solenoid, the coefficients $A_n^{(2)}$ for a given particle velocity v are determined by the boundary condition at the sample position, i.e.:

$$\begin{aligned}
&\sum_n A_n^{(2)} e^{-i\omega_n(B_2)\tau}\ |x_n'^{(2)}\rangle = \sum_n A_n^{(1)} e^{-i\omega_n(B_1)\tau}\ |x_n^{(1)}\rangle \Leftrightarrow \\
&\sum_n A_n^{(2)} e^{-i\omega_n(B_2)\tau}\ |z_n'^{(2)}\rangle = \sum_n A_n^{(1)} e^{-i\omega_n(B_1)\tau}\ |z_n^{(1)}\rangle \\
&\tau \equiv L/v
\end{aligned} \tag{7}$$

The set of linear equations, (7), can be readily solved to yield:

$$\begin{aligned}
A_m^{(2)} &= \sum_n A_n^{(1)} e^{-i\omega_n(B_1)\tau} e^{i\omega_m(B_2)\tau} \langle z_m'^{(2)}|(z_n^{(1)}\rangle = \\
&= \Lambda_{m,m}^{(2)-1}(\tau)\langle z_m'^{(2)}|\left[\sum_n |z_n^{(1)}\rangle \Lambda_{n,n}^{(1)}(\tau)\langle z_n^{(1)}|\right] U(\pi/2)|\Psi(0)\rangle
\end{aligned} \tag{8}$$

Following the beam propagation, starting as a pure state with projection (m_I) along the Z axis at $t = 0$, up to the entrance to the detecting region, i.e. at $t = \tau_3 = \frac{2L}{v} = 2\tau$, the state vector at the detector entrance (see Eq. (5)) takes the form:

$$\begin{aligned}
&|\Psi_2(m_I; t = 2\tau)\rangle = \sum_m A_m^{(2)} \Lambda_{m,m}^{(2)}(2\tau) U(\pi/2)^\dagger |z_m'^{(2)}\rangle = U(\pi/2)^\dagger \times \\
&\times \left[\sum_m |z_m'^{(2)}\rangle \Lambda_{m,m}^{(2)}(\tau)\langle z_m'^{(2)}|\right]\left[\sum_n |z_n^{(1)}\rangle \Lambda_{n,n}^{(1)}(\tau)\langle z_n^{(1)}|\right] U(\pi/2)|\Psi(0)\rangle
\end{aligned} \tag{9}$$

The transition probability through the spin analyzer and correspondingly the count rate at the detector depend on the spin projection of the particle along the detecting field direction $\widehat{Z}'$. To account for the finite velocity distribution of the beam particles, we assume a Gaussian distribution:

$$P(v) = \frac{1}{\sqrt{\pi}\Delta v}\exp[-\frac{(v-\bar{v})^2}{\Delta v^2}]$$

where $\bar{v}$ is the distribution center and Δv is related to the full width half maximum (FWHM) of the distribution, $\Delta v = \frac{FWHM}{2\sqrt{\ln(2)}}$. The detected signal (DS) is therefore given by:

$$DS = \sum_{m_I} g_{m_I} \sum_{m_I'} C_{m_I'} \int dv P(v) \left| \left\langle m_I' \middle| \Psi_2\left(m_I; t = \frac{2L}{v}\right)\right\rangle \right|^2 \tag{10}$$

The averaging over the (initial) pure-states projections m_I in Eq. (10) reflects the absence of coherence in the preparation of the state vector entering the first solenoid. Note that in an ideal experiment the beam should be completely polarized by the first magnetic lens and we will have only one pure initial state. In a realistic experiment we will have a small but finite population starting the experiment with an opposite spin projection, and the summation over initial states allows us to take this into account. In practice, the existence of opposite spin population will simply reduce the polarization and increase the constant component of the measured signal.

To find the detected signal the center of mass velocity v should be integrated out. This can be always done analytically since the velocity dependence shows up only through the exponentials $e^{-i\omega_n(B_j)\tau}$, appearing in:

$$\left|\left\langle m_I'\middle|\Psi_2\left(m_I;t=\tfrac{2L}{v}\right)\right\rangle\right|^2=$$
$$=\left|\langle m_I'|\ U(\pi/2)^{\dagger}\left[\sum_m |z_m'^{(2)}\rangle\Lambda^{(2)}_{m,m}(\tau)\langle z_m'^{(2)}|\right]\times\right.$$
$$\left.\times\left[\sum_n |z_n^{(1)}\rangle\Lambda^{(1)}_{n,n}(\tau)\langle z_n^{(1)}|\right]U(\pi/2)|\Psi(0)\rangle\right|^2 \tag{11}$$

Selecting basis-set vectors, $|z_1\rangle$, $|z_2\rangle$, ..., defined as the eigenvectors of the Zeeman spin Hamiltonian for field orientation parallel to the source magnetic field (Z -axis), the projection $|\langle m_I'|\Psi_2(m_I;t=2\tau)\rangle|^2$can be represented as a product of matrices:

$$\langle m_I'\ \left|\ \Psi_2\left(m_I;t=\tfrac{2L}{v}\right)\right\rangle=$$
$$=\langle m_I'|\ U(\pi/2)^{\dagger}|z_{k_1}\rangle Z'^{(2)}_{k_1,m}\Lambda^{(2)}_{m,m}(\tau)Z'^{(2)-1}_{m,k_2}\times$$
$$\times Z^{(1)}_{k_2,n}\Lambda^{(1)}_{n,n}(\tau)Z^{(1)-1}_{n,k_3}\langle z_{k_3}|\ U(\pi/2)|z_{ini}\rangle \tag{12}$$

where $\Lambda^{(j)}(\tau)$ are the diagonal dynamical matrices:

$$\Lambda^{(j)}_{n,n}(\tau=L/v)=e^{-i\omega_n(B_j)\tau},\text{and}$$
$$Z^{(1)}_{k,n}\equiv\langle z_k\ |z_n^{(1)}\rangle$$
$$Z'^{(1)-1}_{n,k}\equiv\langle z_n'^{(1)}\ |z_k\rangle$$
$$Z'^{(2)}_{k,n}\equiv\langle z_k\ |z_n'^{(2)}\rangle$$
$$Z'^{(2)-1}_{n,k}\equiv\langle z_n'^{(2)}\ |z_k\rangle$$

are the corresponding matrices of eigenvectors, and $|z_{ini}\rangle$ denoting one of the initial states $|z_1\rangle$, $|z_2\rangle$, ... Note that the convention of summing over repeated indices is applied in Eq. (12). Using the rotation transformation from the source quantization (Z) axis to the detector quantization (Z') axis: $|z_m'^{(2)}\rangle=U^{\dagger}(\Theta_B)|z_m^{(2)}\rangle$, $\Theta_B=\frac{3\pi}{4}$, Eq. (12) can be written in the selected basis set representation as:

$$\langle m_I'\ \left|\ \Psi_2\left(m_I;t=\tfrac{2L}{v}\right)\right\rangle=$$
$$=\langle z_{fin}|\ U(\Theta_B)U(\pi/2)^{\dagger}U^{\dagger}(\Theta_B)Z^{(2)}\Lambda^{(2)}(\tau)Z^{(2)-1}U(\Theta_B)\times$$
$$\times Z^{(1)}\Lambda^{(1)}(\tau)Z^{(1)-1}U(\pi/2)|z_{ini}\rangle \tag{13}$$

where the detector pure state, $|m_I'\rangle$, is represented in the reference frames of the source through the $Z\longrightarrow Z'$ quantization-axis rotation, i.e. $|m_I'\rangle=|z_{fin}'\rangle=U^{\dagger}(\Theta_B)|z_{fin}\rangle$, and $|z_{fin}'\rangle$ denoting one of the final states $|z_1'\rangle$, $|z_2'\rangle$,.... Continuing the calculation from this point explicitly with the spin 1/2 model, we select $|z_1\rangle=\begin{pmatrix}1\\0\end{pmatrix}$, $|z_2\rangle=\begin{pmatrix}0\\1\end{pmatrix}$, and use the spin 1/2 Wigner matrix, $U(\Theta_B)=\begin{pmatrix}\cos\frac{\Theta_B}{2} & -\sin\frac{\Theta_B}{2}\\ \sin\frac{\Theta_B}{2} & \cos\frac{\Theta_B}{2}\end{pmatrix}$, for rotation with angle Θ_B about the Y-axis, so that:

$$|z_1'\rangle=U^{\dagger}(\Theta_B)|z_1\rangle=\begin{pmatrix}\cos\frac{\Theta_B}{2}\\ -\sin\frac{\Theta_B}{2}\end{pmatrix}$$
$$|z_2'\rangle=U^{\dagger}(\Theta_B)|z_2\rangle=\begin{pmatrix}\sin\frac{\Theta_B}{2}\\ \cos\frac{\Theta_B}{2}\end{pmatrix}$$
$$Z^{(2)}=Z^{(1)}=\begin{pmatrix}1 & 0\\ 0 & 1\end{pmatrix}$$
$$\Lambda^{(j)}(\tau)=\begin{pmatrix}e^{i(\gamma/2)Bj\tau} & 0\\ 0 & e^{-i(\gamma/2)Bj\tau}\end{pmatrix},\ j=1,\ 2.$$

It is then easy to show that:

$$\langle m_I'|\Psi_2(m_I;t=2\tau)\rangle=$$
$$=\langle z_{fin}|\ U(\pi/2)^{\dagger}\Lambda^{(2)}(\tau)U(\Theta_B)\Lambda^{(1)}(\tau)U(\pi/2)|z_{ini}\rangle,$$

yielding:

$$\left\langle (1/2)'\middle|\Psi_2\left(1/2;t=\tfrac{2L}{v}\right)\right\rangle=\cos\left(\tfrac{\Theta_B}{2}\right)\cos[\tau(\gamma/2)(B_1+B_2)]+$$
$$+i\sin\left(\tfrac{\Theta_B}{2}\right)\sin[\tau(\gamma/2)(B_1-B_2)] \tag{14}$$

for the pair of initial and final spin projections $m_I=1/2$, $m_I'=(1/2)'$, respectively, dominating the measured signal (see below for more details). Matrix elements for the other pairs of initial and final states are presented in Appendix B. For the special case where the second solenoid arm smoothly follows the first one, i.e. for $\Theta_B=0$, Eq. (14) produces an anti-parallel spin echo at $B_2=-B_1$, associated with the cancellation of the phases, $(\gamma/2)B_1\tau$, $-(\gamma/2)B_1\tau$, accumulated during spin precession in the first solenoid, by the respective phases, $(\gamma/2)B_2\tau$, $-(\gamma/2)B_2\tau$, accumulated in the second solenoid, regardless of the particle velocity v. However, for any $\Theta_B>0$, the nonzero term proportional to $\sin\left(\frac{\Theta_B}{2}\right)$ in Eq. (14) allows for an additional, parallel echo at $B_2=B_1$. The origin of the two different echoes can be revealed by considering the propagators product:

$$\Lambda^{(2)}(\tau)U(\Theta_B)\Lambda^{(1)}(\tau)=$$
$$=\begin{pmatrix}\cos\frac{\Theta_B}{2}e^{i\tau(\gamma/2)B_1}e^{i\tau(\gamma/2)B_2} & -\sin\frac{\Theta_B}{2}e^{-i\tau(\gamma/2)B_1}e^{i\tau(\gamma/2)B_2}\\ \sin\frac{\Theta_B}{2}e^{i\tau(\gamma/2)B_1}e^{-i\tau(\gamma/2)B_2} & \cos\frac{\Theta_B}{2}e^{-i\tau(\gamma/2)B_1}e^{-i\tau(\gamma/2)B_2}\end{pmatrix} \tag{15}$$

appearing in Eq. (13). The diagonal elements of the rotation matrix $U(\Theta_B)$, operating between the propagators $\Lambda^{(2)}(\tau)$, $\Lambda^{(1)}(\tau)$ in the two solenoids, mix the wavefunction components; $e^{i(\gamma/2)B_1\tau}$, $e^{-i(\gamma/2)B_1\tau}$, in the first solenoid, with the respective components; $e^{i(\gamma/2)B_2\tau}$, $e^{-i(\gamma/2)B_2\tau}$, in the second solenoid, thus leading to the first term on the RHS of Eq. (14), with echo at $B_2=-B_1$. On the other hand, the off-diagonal elements of the rotation matrix $U(\Theta_B)$, which are responsible for the mixing of the wavefunction components; $e^{i(\gamma/2)B_1\tau}$, $e^{-i(\gamma/2)B_1\tau}$ with the respective reflected wave function components; $e^{-i(\gamma/2)B_2\tau}$, $e^{i(\gamma/2)B_2\tau}$, lead to the second term on the RHS of Eq. (14), with echo at $B_2=B_1$. These wavefunction reflections in spin space are induced by the fast rotation of the magnetic field direction in the transition region between the two solenoids, following the particle center-of-mass reflection at the sample surface. The corresponding non-adiabatic nature of the spin dynamics in the transition region is responsible for the spin-flip process with precession energy difference $(\gamma/2)(B_2-B_1)$, appearing in the parallel echo term in Eq. (14). Mathematically, it is related to the fact that the spin Hamiltonians at times just before and after the magnetic field rotation do not commute.

The experimentally measured signal, Eq. (10), is now obtained by averaging $\left|\left\langle m_I'\middle|\Psi_2\left(m_I;t=\frac{2L}{v}\right)\right\rangle\right|^2$ over the velocity distribution. Since the initial state populations g_{m_I} (determined by quantum state selector) and detection probabilities $C_{m_I'}$ satisfy $g_{1/2}\gg g_{-1/2}$ and $C_{(1/2)'}\gg C_{(-1/2)'}$, respectively, the detected signal is dominated by the pair of initial and final spin projections $m_I=1/2$, $m_I'=(1/2)'$, namely:

$$DS\approx\overline{\left|\left\langle (1/2)'\middle|\Psi_2\left(1/2;t=\tfrac{2L}{v}\right)\right\rangle\right|^2}=$$
$$\cos^2\tfrac{\Theta_B}{2}\overline{\cos^2[\tau(\gamma/2)(B_1+B_2)]}+$$
$$+\sin^2\left(\tfrac{\Theta_B}{2}\right)\overline{\sin^2[\tau(\gamma/2)(B_1-B_2)]}\approx$$
$$\approx\cos^2\left(\tfrac{\Theta_B}{2}\right)\left[\tfrac{1}{2}+\tfrac{1}{2}e^{-\left(\frac{\Delta v}{\bar v}\right)^2\left(\frac{\gamma(B_1+B_2)L}{2\bar v}\right)^2}\cos\left(\tfrac{\gamma(B_1+B_2)L}{\bar v}\right)\right]+$$
$$+\sin^2\left(\tfrac{\Theta_B}{2}\right)\left[\tfrac{1}{2}-\tfrac{1}{2}e^{-\left(\frac{\Delta v}{\bar v}\right)^2\left(\frac{\gamma(B_1-B_2)L}{2\bar v}\right)^2}\cos\left(\tfrac{\gamma(B_1-B_2)L}{\bar v}\right)\right] \tag{16}$$

Components of measured signal for other pairs of initial and final states are again presented in Appendix B. Thus, under the anti-parallel echo condition, $B_1=-B_2\equiv B$ the dominant transition probability is given by:

$$\overline{\left|\left\langle (1/2)'\left|\Psi_2\left(1/2;t=\frac{2L}{v}\right)\right\rangle\right|^2}_{B_1+B_2=0} =$$
$$= \cos^2\frac{\Theta_B}{2} + \frac{1}{2}\sin^2\frac{\Theta_B}{2}\left[1 - e^{-\left(\frac{\Delta v}{\bar{v}}\right)^2\left(\frac{\gamma BL}{\bar{v}}\right)^2}\cos\left(\frac{2\gamma BL}{\bar{v}}\right)\right]\approx$$
$$\approx \cos^2\frac{\Theta_B}{2} + \frac{1}{2}\sin^2\frac{\Theta_B}{2} \tag{17}$$

where the approximate equality usually holds due to a very small Gaussian factor. Note that this requires the fields to be sufficiently large, in which case we obtain a dephasing of the signal far away from the spin echo condition.

Similarly, under the parallel echo condition, $B_2 = B_1 \equiv B$, we find:

$$\overline{\left|\left\langle (1/2)'\left|\Psi_2\left(1/2;t=\frac{2L}{v}\right)\right\rangle\right|^2}_{B_1-B_2=0} =$$
$$= \frac{1}{2}\cos^2\frac{\Theta_B}{2}\left[1 + e^{-\left(\frac{\Delta v}{\bar{v}}\right)^2\left(\frac{\gamma BL}{\bar{v}}\right)^2}\cos\left(\frac{2\gamma BL}{\bar{v}}\right)\right]\approx$$
$$\approx \frac{1}{2}\cos^2\frac{\Theta_B}{2} \tag{18}$$

Reverting to the definitions introduced above, the parallel and anti-parallel magnetic field configurations produce detectable oscillations, as functions of $\Delta B_{\mp} = B_1 \mp B_2$, whose envelope intensities scale like $\sin^2\left(\frac{\Theta_B}{2}\right)$ and $\cos^2\left(\frac{\Theta_B}{2}\right)$ respectively (see Eq. (16)). Thus in the limiting case of extremely sharp total scattering angles ($\Theta_{tot} \to 0°$, $\Theta_B \to 180°$), we expect only parallel echoes. In contrast, in the extreme case of a straight through apparatus ($\Theta_{tot} \to 180°$, $\Theta_B \to 0°$) we expect a vanishing parallel echo (unless we use a spin flipper which can increase the intensity of an anti-parallel echo). Most importantly, in the general case we expect both echoes to exist with a relative intensity which reflects the actual scattering angle used in the experiment.

Classical versus quantum descriptions

An important test of the results presented in the previous section is made here by applying classical magneto dynamics to the spin echo experiment described in this paper. Starting with the classical equation of motion for a magnetic moment $\vec{\mu}$ in an external magnetic field $\vec{B}$,

$$\frac{d}{dt}\vec{\mu} = \gamma[\vec{\mu} \times \vec{B}] \tag{19}$$

where γ is the gyromagnetic ratio, we consider three stages of the particle propagation in the experimental setup: (1) free flight of particles in solenoid 1, with a constant velocity $\vec{v} = v\hat{X}$, (2) reflection from the sample surface (total scattering angle $\Theta_{tot} = 180° - \Theta_B$), and (3) free flight of particles in solenoid 2, with a constant velocity $\vec{v}' = v\hat{X}'$. Scattering is assumed to be elastic, $v = v'$. For spin systems with a pure Zeeman magnetic interaction, addition of free-field regions (existing in a real experimental system) to propagation diagram does not affect the precession-induced phase acquired during particle propagation, so that these regions are excluded. Choice of coordinate axes and direction of magnetic field in both solenoids are shown below.

A particle, with an initial magnetic moment at the entrance: $\vec{\mu}_0 = \mu_{y0}\hat{Y} + \mu_{z0}\hat{Z}$, is moving through solenoid 1 during the time interval $t_0 \leqslant t \leqslant t_1$. Its initial magnetic moment component parallel to magnetic field in solenoid 1 does not change, and so does not participate in formation of spin echo signal. We, therefore assume, without loss of generality, that $\mu_{x0} = 0$. The equations of motion for the magnetic-moment components in solenoid 1 are then written as:

$$\dot{\mu}_y = \gamma\mu_z B_1(x),\ \dot{\mu}_z = -\gamma\mu_y B_1(x) \tag{20}$$

with their solutions, in general form:

$$\mu_y(t) = \mu_{\perp 0}\sin\left[F_1(vt)\frac{\gamma}{v} + \varphi_0\right],$$
$$\mu_z(t) = \mu_{\perp 0}\cos\left[F_1(vt)\frac{\gamma}{v} + \varphi_0\right] \tag{21}$$

where $\mu_{\perp 0} = \sqrt{\mu_{y0}^2 + \mu_{z0}^2}$, and $F_1(vt) \equiv \int_{vt_0}^{vt} B_1(x)dx$. Assuming, for simplicity, a rectangular magnetic field profile we have: $F_1(vt) = B_1 v(t - t_0)$. Thus, at the end of solenoid 1 one finds:

$$\mu_y(t_1) = \mu_{\perp 0}\sin\left(F_1\frac{\gamma}{v} + \varphi_0\right),$$
$$\mu_z(t_1) = \mu_{\perp 0}\cos\left(F_1\frac{\gamma}{v} + \varphi_0\right) \tag{22}$$

where $F_1 \equiv B_1 L$.

Similarly, the solutions for the magnetic moment components in solenoid 2, during the time interval $t_2 \leqslant t \leqslant t_3$, is written, in the primed reference of frames, as:

$$\mu_{y'}(t) = \mu_y(t) = \mu'_{\perp 0}\sin\left[F_2(vt)\frac{\gamma}{v} + \varphi_2\right],$$
$$\mu_{z'}(t) = \mu'_{\perp 0}\cos\left[F_2(vt)\frac{\gamma}{v} + \varphi_2\right] \tag{23}$$

where $F_2(vt) = B_2 v(t - t_2)$. The phase φ_2 for evolution of the magnetic moment in the second coil can be found from the matching conditions at $t_1 = t_2$:

$$\mu_y(t_1) = \mu_{\perp 0}\sin\left(F_1\frac{\gamma}{v} + \varphi_0\right) = \mu_y(t_2) = \mu'_{\perp 0}\sin(\varphi_2), \tag{24}$$

$$\mu_{z'}(t_1) = \mu_z(t_1)\cos\Theta_B = \mu_{\perp 0}\cos\Theta_B\cos\left(F_1\frac{\gamma}{v} + \varphi_0\right) = \mu_{z'}(t_2) = \mu'_{\perp 0}\cos(\varphi_2) \tag{25}$$

Exploiting the above matching conditions for expressing φ_2 in terms of $\mu_y(t_2)$, $\mu_{z'}(t_2)$, and $\mu'_{\perp 0}$, we can further use them for calculating φ_2 in terms of the reflection angle Θ_B and the phase $F_1\frac{\gamma}{v} + \varphi_0$ acquired by a particle during precession in the first coil, i.e.:

$$\sin\varphi_2 = \frac{\sin\left(F_1\frac{\gamma}{v} + \varphi_0\right)}{\sqrt{\sin^2\left(F_1\frac{\gamma}{v} + \varphi_0\right) + \cos^2\Theta_B\cos^2\left(F_1\frac{\gamma}{v} + \varphi_0\right)}} \tag{26}$$

$$\cos\varphi_2 = \frac{\cos\Theta_B\cos\left(F_1\frac{\gamma}{v} + \varphi_0\right)}{\sqrt{\sin^2\left(F_1\frac{\gamma}{v} + \varphi_0\right) + \cos^2\Theta_B\cos^2\left(F_1\frac{\gamma}{v} + \varphi_0\right)}} \tag{27}$$

The matching conditions, Eqs. (24) and (25), also yield the relation:

$$\mu'_{\perp 0} = \mu_{\perp 0}\sqrt{\sin^2\left(F_1\frac{\gamma}{v} + \varphi_0\right) + \cos^2\Theta_B\cos^2\left(F_1\frac{\gamma}{v} + \varphi_0\right)} \tag{28}$$

Thus, combining common trigonometric expansions with Eqs. (26)–(28) we find explicit expressions for $\mu_y(t_3)$, $\mu_{z'}(t_3)$ in terms of F_1, $F_2 \equiv B_2 L$, φ_0 and Θ_B, namely:

$$\mu_y(t_3) = \mu'_{\perp 0}\sin(F_2\frac{\gamma}{v} + \varphi_2) =$$
$$= \mu_{\perp 0}\left[\sin\left(F_2\frac{\gamma}{v}\right)\cos\Theta_B\cos\left(F_1\frac{\gamma}{v} + \varphi_0\right) + \right.$$
$$\left. + \cos\left(F_2\frac{\gamma}{v}\right)\sin\left(F_1\frac{\gamma}{v} + \varphi_0\right)\right]$$

$$\mu_{z'}(t_3) = \mu'_{\perp 0}\cos\left(F_2\frac{\gamma}{v} + \varphi_2\right) =$$
$$= \mu_{\perp 0}\left[\cos\left(F_2\frac{\gamma}{v}\right)\cos\Theta_B\cos\left(F_1\frac{\gamma}{v} + \varphi_0\right) - \right.$$
$$\left. - \sin\left(F_2\frac{\gamma}{v}\right)\sin\left(F_1\frac{\gamma}{v} + \varphi_0\right)\right]$$

which can be rewritten in terms of $B_1 + B_2$ and $B_1 - B_2$ as:

$$\mu_y(t_3) = \mu_{\perp 0}\left\{\cos^2\frac{\Theta_B}{2}\sin\left[\gamma\left(B_1 + B_2\right)\frac{L}{v} + \varphi_0\right] + \sin^2\frac{\Theta_B}{2}\sin\left[\gamma\left(B_1 - B_2\right)\frac{L}{v} + \varphi_0\right]\right\} \tag{29}$$

$$\mu_{z'}(t_3) = \mu_{\perp 0}\left\{\cos^2\frac{\Theta_B}{2}\cos\left[\gamma\left(B_1 + B_2\right)\frac{L}{v} + \varphi_0\right] - \sin^2\frac{\Theta_B}{2}\cos\left[\gamma\left(B_1 - B_2\right)\frac{L}{v} + \varphi_0\right]\right\} \tag{30}$$

For comparison with the quantum results derived in the previous section we should evaluate the expectation value of the time dependent magnetic moment for the spin $I = 1/2$ case by using the results of the probabilities $P_{m_I',m_I}(\Theta_B) \equiv |\langle m_I'\ |\Psi_2(m_I;t = 2L/v)\rangle|^2$ calculated from Eq. (13). Thus, we find for the pure initial projection $m_I = 1/2 \leftrightarrow |z_1\rangle$ and the pure final projections $m_I' = 1/2, -1/2 \leftrightarrow |z_1'\rangle, |z_2'\rangle$:

$$P_{11}(\Theta_B) = P_{22}(\Theta_B) = = \cos^2\frac{\Theta_B}{2}\cos^2\frac{G^+}{2} + \sin^2\frac{\Theta_B}{2}\sin^2\frac{G^-}{2} \tag{31}$$

$$P_{12}(\Theta_B) = P_{21}(\Theta_B) = = \cos^2\frac{\Theta_B}{2}\sin^2\frac{G^+}{2} + \sin^2\frac{\Theta_B}{2}\cos^2\frac{G^-}{2} \tag{32}$$

where $G^{\pm} = \gamma(B_1 \pm B_2)\frac{L}{v}$ (note Eq. (14) for the $|z_1\rangle \rightarrow |z_1'\rangle$ transition amplitude), yielding for the expectation value:

$$\langle\mu_{z'}\rangle = \frac{1}{2}\hbar\gamma\left[P_{11}(\Theta_B) - P_{21}(\Theta_B)\right] = \frac{1}{2}\hbar\gamma\left(\cos^2\frac{\Theta_B}{2}\cos G^+ - \sin^2\frac{\Theta_B}{2}\cos G^-\right) \tag{33}$$

in full agreement with the corresponding classical result, Eq. (30).

For interpretation of experimental results, the inverse relations can be useful

$$P_{z_1'} = \frac{1}{2}\left(1 + \frac{2\langle\mu_{z'}\rangle}{\hbar\gamma}\right),\ P_{z_2'} = \frac{1}{2}\left(1 - \frac{2\langle\mu_{z'}\rangle}{\hbar\gamma}\right) \tag{34}$$

where $P_{z_1'}$ and $P_{z_2'}$ are probabilities for a particle to be found at the detection point in states $|z_1'\rangle$ and $|z_2'\rangle$, respectively. Furthermore, applying the quantum approach developed in the previous section for higher spins, we find e.g. for spin $I = 1$:

$$P_{11}(\Theta_B) = P_{33}(\Theta_B) = \left(\cos^2\frac{\Theta_B}{2}\cos^2\frac{G^+}{2} + \sin^2\frac{\Theta_B}{2}\sin^2\frac{G^-}{2}\right)^2 \tag{35}$$

$$P_{31}(\Theta_B) = P_{13}(\Theta_B) = \left(\cos^2\frac{\Theta_B}{2}\sin^2\frac{G^+}{2} + \sin^2\frac{\Theta_B}{2}\cos^2\frac{G^-}{2}\right)^2 \tag{36}$$

which yield the following average magnetic moment for the pure initial projection $m_I = 1$:

$$\langle\mu_{z'}\rangle = \hbar\gamma\left[P_{11}(\Theta_B) - P_{31}(\Theta_B)\right] = = \frac{\hbar\gamma}{2}\left[(1 + \cos\Theta_B)\cos G^+ - (1 - \cos\Theta_B)\cos G^-\right] = = \hbar\gamma\left[\cos^2\frac{\Theta_B}{2}\cos G^+ - \sin^2\frac{\Theta_B}{2}\cos G^-\right] \tag{37}$$

in full agreement with the spin 1/2 result, Eq. (33). Here the basis-set vectors are: $|z_1\rangle \leftrightarrow m_I = 1$, $|z_2\rangle \leftrightarrow m_I = 0$, and $|z_3\rangle \leftrightarrow m_I = -1$.

Numerical classical calculations of parallel and anti-parallel echoes

While the quantum and classical analytic approaches described above are insightful, the experimental apparatus often contains a more complex magnetic field arrangement including additional intentional and unintentional magnetic fields as well as realistic (i.e. not infinitely sharp) magnetic field profiles. For these cases a numerical solution is helpful. One example is the additional spin rotator coil (typically termed spin flipper in NSE) which is located before the sample (see Fig. 1). We used a numerical solution of Eq. (20) to calculate the parallel and anti-parallel echoes with and without the spin rotator field. The spin evolution is calculated classically by introducing a time dependent magnetic field in Eq. (20). This magnetic field reflects the field experienced by the particle, within the particle frame of reference, as it propagates through the instrument.

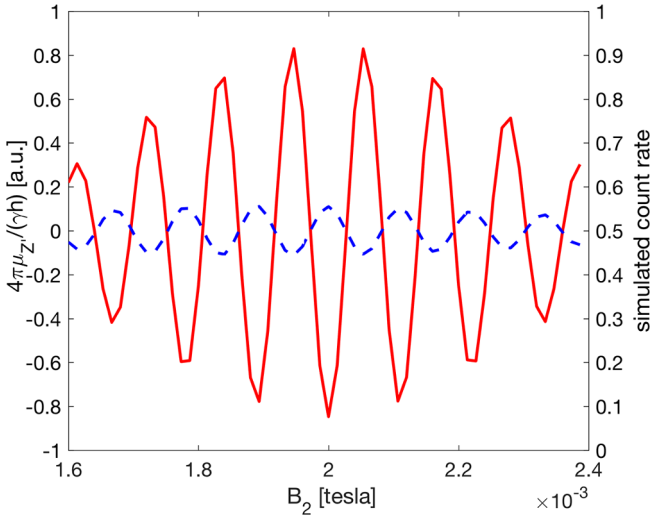

Fig. 2. Parallel (solid red line) and anti-parallel (dashed blue line) spin echoes, calculated by the numerical solution of equation 20, for a total scattering angle of 45°. B_1 was set at a fixed value of $2{\cdot}10^{-3}$ tesla and B_2 was scanned around B_1 or around $-B_1$. The left vertical axis shows the magnetic moment along the detection axis, Z', whereas the right vertical axis shows the corresponding detection count rate.

Fig. 2 shows a calculation performed for a scattering experiment with a total scattering angle of 45° which follows the layout shown in Fig. 1. The simulated signal was calculated using 100 spins with velocities distributed ±10% around a mean velocity of 717 m/s. The red line shows the parallel spin echo and the blue line shows the anti-parallel echo. As expected from the analytic derivation the parallel echo is stronger for sharp Θ_{tot} values, but the anti-parallel echo is definitely not negligible. At the center of the echoes ($|B_1| = |B_2|$), the simulated average magnetic-moment (left vertical axis) reproduces the values given in Eq. (30) for $\Theta_{tot} = 45°$. The right vertical axis displays the (normalized) simulated count rate $P_{z_1'}$ (see Eq. (34)).

Using the spin rotator coil to rotate the spins by 45° one can enhance the parallel echo even further, and indeed this type of rotation has been used to improve the polarization in HSE experiments [21]. The term polarization is often used to quantify the oscillating fraction of the signal in a way which is independent of the signal intensity and any constant background due to unpolarized spins, polarization $= \frac{\max\left(P_{z_1'}\right) - \min\left(P_{z_1'}\right)}{\max\left(P_{z_1'}\right) + \min\left(P_{z_1'}\right)}$. Fig. 3 shows the numerically calculated polarization for different rotations in the spin-rotator coil. A 45° rotation simultaneously increases the polarization of the parallel echo while reducing the polarization of the anti-parallel echo, however, as can be seen in the figure, the spin rotator can also be used to completely reverse the relative intensities of the two echoes.

Fig. 4 shows a calculation of the parallel echo for an obtuse scattering angle configuration. Here $\Theta_{tot} = 150°$ and the angle between the two magnetic fields is only 30°. In this case, the parallel echo (blue line) is quite small since B_1 and B_2 are almost parallel. An extra rotation with the spin rotator can be used to increase the parallel echo signal. The red line shows an example using a spin rotation angle of 180°.

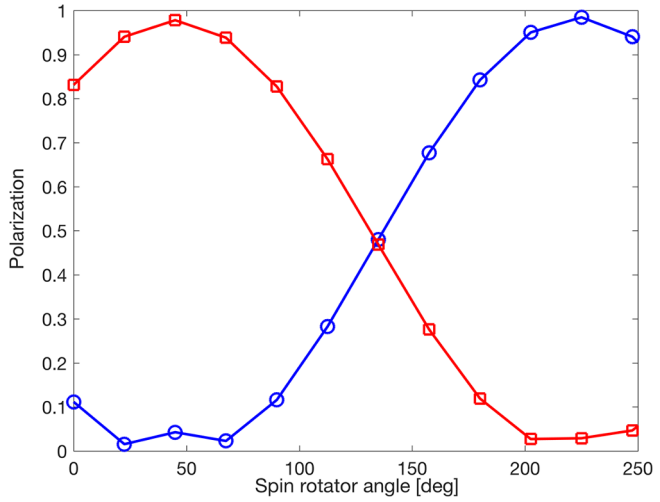

Fig. 3. Simulated polarization for the parallel and anti-parallel echoes (red squares/blue circles) as function of the rotation angle in the spin rotator coil. (For interpretation of the references to colour in this figure legend, the reader is referred to the web version of this article.)

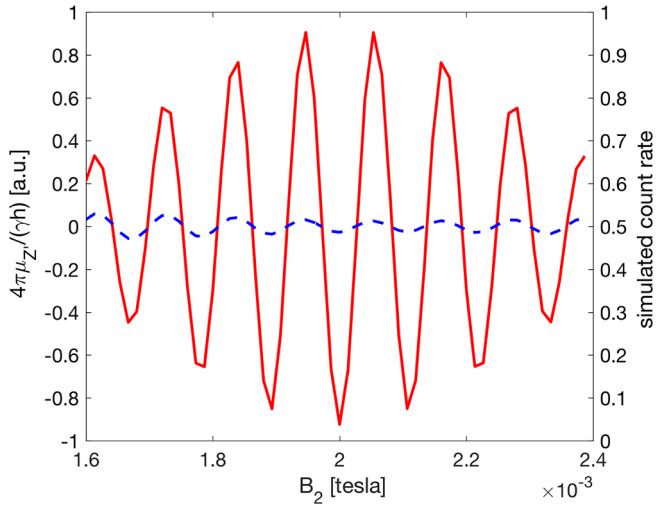

Fig. 4. Parallel spin echoes calculated by the numerical solution of equation 20, for a total scattering angle of 150° ($\Theta_B = 30°$). B_1 was set at a fixed value of $2{\cdot}10^{-3}$ tesla and B_2 was scanned around B_1 with the spin rotator set to 180° (solid red line) and with the spin rotator off (dashed blue line). (For interpretation of the references to colour in this figure legend, the reader is referred to the web version of this article.)

Measurements of the two echoes, with and without an additional rotator coil

An experimental demonstration of the simultaneous existence of parallel and anti-parallel echoes is shown in Fig. 5. The measurements were performed using a helium-3 beam produced with a 1 bar pressure behind a 20 micron nozzle cooled to 34 K. The sample was a vacuum cleaved NaCl crystal set at specular scattering conditions and oriented along the $\langle 100 \rangle$ crystal azimuth.

The HSE setup we used has a fixed total scattering angle of 45° between the source and detector, i.e. the relative angle between the axes of the two magnetic fields is 135°, the initial polarization is along the Z axis and the detection axis is along the $-Z'$ axis (see Fig. 1 for axes definitions). The red cross markers show the results measured in a parallel magnetic field configuration and the blue circle markers show the anti-parallel configuration, achieved by reversing the current in B_1 . As expected for a sharp total scattering angle, the parallel echoes are more intense but nevertheless the anti-parallel echoes are clearly observed.

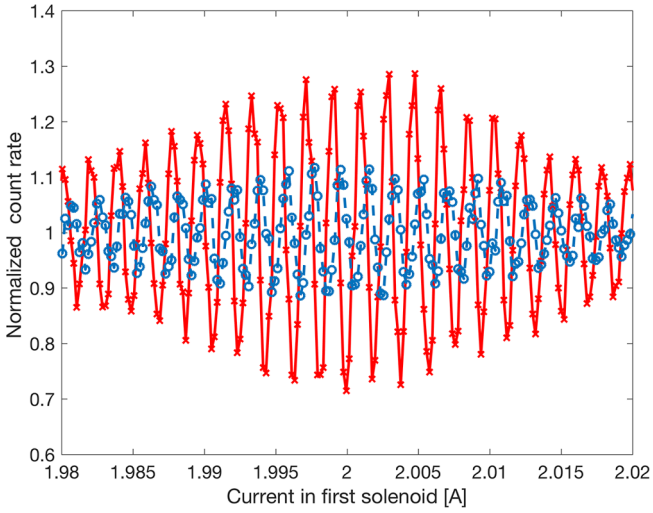

Fig. 5. Parallel and anti-parallel echoes. The solenoid coil producing the second magnetic field was set at a fixed current value ($I_2 = 2A$ and $I_2 = -2A$) and the current in the first field was scanned around $I_1 = 2A$. The red line shows the results when scanning around the condition $I_1 = I_2$ and the blue lines show the measurements when scanning around $I_1 = -I_2$. The results were normalized with respect to the constant signal level.

As mentioned above, the spin rotator coil can be used to alter the relative intensity of the parallel and anti-parallel echoes. The spin rotator coil we used was a helmholtz pair positioned at the entrance to the scattering chamber producing a field along the Y axis (Fig. 1). The three panels in Fig. 6 show the polarization of the two echoes as function of current in the spin rotator coil, reproducing the trends seen in the

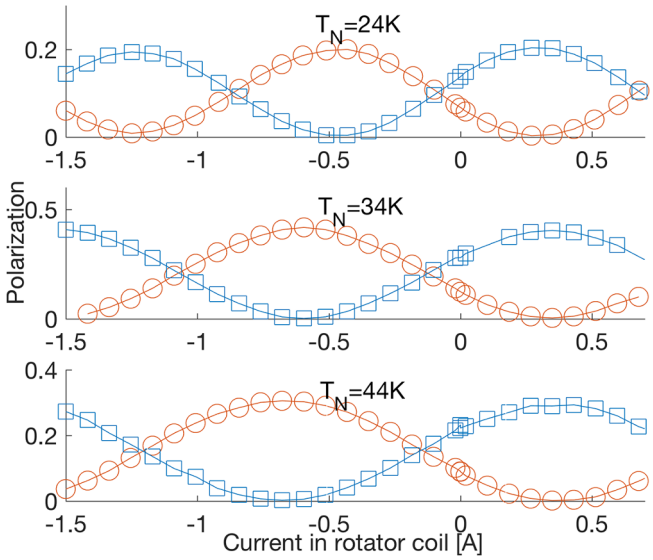

Fig. 6. Comparing the polarization of the parallel and anti-parallel echo signals (blue squares and red circles respectively). The polarization of the echoes was measured for different currents in the spin rotator coil (see figure 1), the other experimental conditions were identical to those used to measure the data shown in figure 2 with the exception of the nozzle temperature which was varied between 24 K, 34 K and 44 K (upper, middle and lower panels). As expected the spin rotator can be used to shift the relative intensity between the two echoes and the optimal spin rotator current for measuring the $B_1 = B_2$ echo (red markers) produces a minimum in the $B_1 = -B_2$ echo (blue markers). The lines represent sinusoidal fits to the two sets of data. (For interpretation of the references to colour in this figure legend, the reader is referred to the web version of this article.)

numerical simulations (Fig. 3). The upper, middle and lower panels show results using three different nozzle temperatures, 24 K, 34 K and 44 K, corresponding to average beam speeds of 577, 686 and 781 m/s.

When carefully comparing the experimental data shown in Figs. 5 and 6 with the analytical and numerical results described above there are two interesting discrepancies between the theory and experiment. One is the relative phase difference seen between the signals of the parallel and anti-parallel echoes as function of the current in B_2 (Fig. 5), where we expected a 180° difference and measure a smaller phase difference (≈ 100°). A second discrepancy is the phase of the sinusoidal dependency of the parallel and anti-parallel polarization on the field (current) of the spin rotation coil (Fig. 6), where we expect a maximal/minimal polarization of the parallel/anti-parallel echoes at a rotation angle of 45° and the experimental curves reach the extrema value at larger phase values (changing gradually from 64° to 71° as the nozzle is cooled).

Both of these deviations from the theoretical results can be explained by small residual magnetic fields in between the B_1 and B_2 fields, which become more significant as the beam is slowed down and the particles spend more time in the residual field region (time which is proportional to $\frac{1}{\sqrt{T}}$). Fig. 7 demonstrates this for the case of the phase difference between the parallel and anti-parallel echoes. The blue circles mark the phase differences extracted from experiments with nozzle temperatures of 24 K, 34 K and 44 K. The phase difference as function $\frac{1}{\sqrt{T}}$ behaves linearly (dashed line shows linear fit) and has an intercept of π confirming that for high enough velocities the experiment converges with the expected phase difference in the absence of any additional magnetic fields.

In fact, identifying residual magnetic fields within the non-adiabatic region is a first practical application of the concept of parallel and anti-parallel echoes, and offers unique quantitative insight into the actual magnetic profile the beam particles experience while passing through the experimental apparatus. To isolate the different possible Z, X and Y components of the residual fields the phase difference and relative polarization of parallel and anti-parallel echoes needs to be measured by scanning B_1, B_2 and the spin rotator field respectively. To obtain numerical values for the residual fields from the experimental data we fit the experimental results with the numerical simulation described earlier. Fig. 7 demonstrates such a fit, where the green square markers show the results of the numerical simulation where we include a small residual field along the Z axis with a magnetic field path integral of $1.7{\cdot}10^{-6}$ Tm (equivalent to a 2 gauss field which is 1 cm long). Similarly, the phase shifts seen in Fig. 6 can be attributed to a residual field of $1.3{\cdot}10^{-6}$ Tm along the Y axis. The origin of these small field components might be remnant magnetization in the 304 stainless steel of the sample holder, a possibility that will be further investigated. While these residual fields are much smaller than the maximal fields we typically use in B_1 and B_2 (which can be as strong as $0.1Tm$ in our apparatus), they need to be taken into account during the data interpretation of spin echo measurements when the phase of the signal is included in the data analysis.

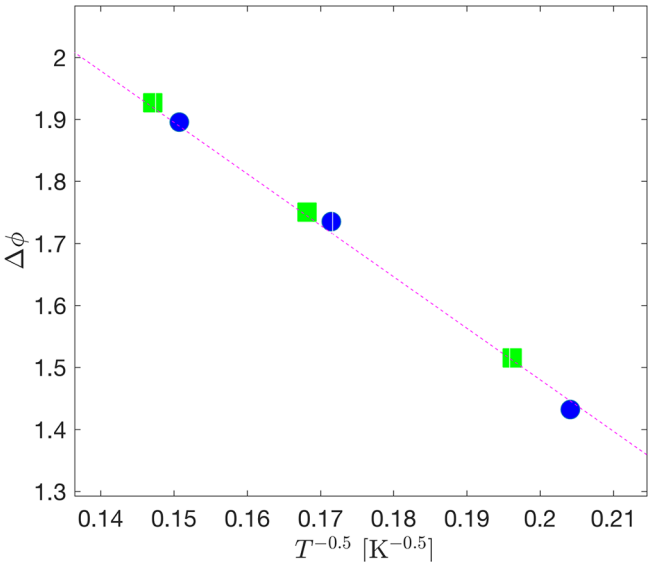

Fig. 7. Phase difference (in radians) between parallel and anti-parallel echo signals. The blue circle markers show measurements of the phase difference where the B_1 field was scanned and B_2 was set at fixed values with opposite polarity to obtain parallel and anti-parallel echoes. The $\frac{1}{\sqrt{T}}$ dependence follows a linear dependence with a intercept of π and a slope of $8.3\text{K}^{-0.5}$ (dashed magenta line). The green squares show numerical simulation results which reproduce the experimental results when a Z field of $1.7{\cdot}10^{-6}$ Tm is added in the non-adiabatic transition region. (For interpretation of the references to colour in this figure legend, the reader is referred to the web version of this article.)

Summary

We have shown in this paper that the fundamental mechanism, controlling the echo phenomenon in beam spin echo setups with non-adiabatic transitions, splits into two channels of constructive interference between the spin-phases accumulated during the beam propagation in the two-coil arms. The first is the commonly studied channel, corresponding to anti-parallel magnetic fields before and after the scattering event, which can lead to echo conditions even for spin dynamics that follow adiabatically the entire particle center-of mass motion. The second, more intriguing channel, which corresponds to parallel magnetic fields before and after the scattering event, is exclusively associated with the non-adiabatic nature of the spin dynamics under rotation of the magnetic field axis in the transition region between the two propagation arms.

We have derived the two spin echo conditions and calculated their relative intensities both quantum mechanically and classically. We also presented measurements of the two echoes and demonstrated how their relative intensities, which depend on the relative angle between the two magnetic fields, can be modified using a spin-rotation coil before the scattering event.

A first practical application of the parallel echo was demonstrated, where we showed that subtle residual magnetic fields in the sample region can be identified, using the measured relative phase and polarization of the two echoes. A different situation where it is important to use a theory which allows for both type of echoes is molecular interference measurements [6]. In further measurements of the same system, multiple spin echoes were measured, related to the complexity of systems with spin >1/2 [22]. To correctly account for these echoes and to interpret the molecule-surface interaction from their spectrum, the full theory which is presented in this paper is needed. Finally, it is important to be aware that non-adiabatic transitions (in our theory the non-adiabatic dynamics is associated with the quick rotation of the external magnetic field axis as seen in the particle reference of frame) lead to significant parallel echo intensities, and that these depend on the geometry of the instrument. For example, in magnetic scattering NSE experiments, an echo can be obtained without using a flipper coil, this is because the sample itself can act as a spin flipper [1]. In this case the observed signal, which is essentially what we refer to as a parallel echo, is solely attributed to magnetic scattering. If magnetic scattering experiments are performed in systems with non-adiabatic transitions along the beam line, there will be additional contributions to the parallel echo intensity related to the non-adiabatic transition mechanism highlighted in this paper, and both mechanisms will contribute to the parallel echo signal. A full theory which includes the precise geometry of the instrument needs to be used to avoid misinterpretation of the data.

Acknowledgements

The authors would like to thank Dr. Peter Fouquet and Mr. Joshua T. Cantin for their insightful comments. This work was funded by the European Research Council under the European Union's seventh framework program (FP/2007-2013)/ERC grant 307267, Horizon 2020 Research and Innovation Programme grant 772228 and the Israel Science Foundation (grant 755/16).

Appendix A

In this appendix we will justify the use of the time–dependent quantum spin picture moving between two time zones, as presented in Sec.II, by showing that, to a very good approximation, it is equivalent to a space-time wave packet representation, constructed from the Stern-Gerlach split wavenumbers generated in the transition region between the corresponding two magnetic field zones.

The state vector, $|\Psi(x,\,t)\rangle$, describing the particles' beam in a field zone is expanded as a Gaussian wavepacket-its center running with velocity v_n in real space-and in the eigenvectors, $|x_n\rangle$, of the spin Hamiltonian with energy eigenvalues, $\hbar\omega_n(B)$, i.e.:

$$|\Psi(x,\,t)\rangle = \sum_n \sqrt{\frac{\sigma}{2}} \int_{-\infty}^{\infty} dk e^{-\frac{1}{2}(k-k_n)^2\sigma} e^{ik(x-v_n t)} a_n(t) e^{-i\omega_n(B)t}\ |x_n\rangle$$

Here σ is the packet width in real space, $k_n = mv_n/\hbar$, m-the particle mass, $|x_n\rangle = U^\dagger\,|z_n\rangle$, where $|z_n\rangle$ are the eigenvectors for the magnetic field orientation in the pre-field-zone region, selected as the Z-axis, and $U^\dagger$ is the unitary transformation associated with the rotation of the magnetic field from the Z-axis to the axis of the wavepacket propagation, i.e. the X-axis. Due to the Stern-Gerlach effect, the packet velocity in the above expression splits according to the magnetic quantum number n. Performing the integration over the wavenumber k (to express the wavepacket as a real space Gaussian), and denoting:

$$A_n(x,\,t) \equiv a_n(t) e^{-\frac{(x-v_n t)^2}{\sigma}} e^{ik_n(x-v_n t)}$$

we find:

$$|\Psi(x,\,t)\rangle = \sum_n A_n(x,\,t) e^{-i\omega_n(B)t}\ |x_n\rangle \tag{38}$$

We may further simplify the problem by noting that the spatial splitting of the packet center, $\Delta v_n t$, along the beam axis is much smaller than the length of a field zone, L, and furthermore significantly smaller than the transition region width between two field zones, to justify its neglect in the above expression. Note, however, that we can not neglect the corresponding splitting in the wavenumber k_n since the phase shifts associated with them reflect the Stern-Gerlach effect. Thus we rewrite:

$$A_n(x,\,t) \simeq a_n(t) e^{-\frac{(x-vt)^2}{\sigma}} e^{ik_n(x-vt)} \tag{39}$$

where v is the average velocity of the split wavepacket centers. For our spin 1/2 particle we have:

$$\omega_1(B) = -(\gamma/2)B,\ \ \omega_2(B) = (\gamma/2)B,$$
$$|z_1\rangle = \begin{pmatrix}1\\0\end{pmatrix},\qquad |z_2\rangle = \begin{pmatrix}0\\1\end{pmatrix},$$
$$U = \frac{1}{\sqrt{2}}\begin{pmatrix}1 & 1\\ -1 & 1\end{pmatrix}$$

and the state vector:

$$|\Psi(x,\,t)\rangle = A_1(x,\,t) e^{-i\omega_1(B)t} \frac{1}{\sqrt{2}}\begin{pmatrix}1 & -1\\ 1 & 1\end{pmatrix}\begin{pmatrix}1\\0\end{pmatrix} + A_2(x,\,t) e^{-i\omega_2(B)t} \frac{1}{\sqrt{2}}\begin{pmatrix}1 & -1\\ 1 & 1\end{pmatrix}\begin{pmatrix}0\\1\end{pmatrix} = \frac{1}{\sqrt{2}}\begin{pmatrix}A_1(x,\,t)e^{-i\omega_1(B)t} - A_2(x,\,t)e^{-i\omega_2(B)t}\\ A_1(x,\,t)e^{-i\omega_1(B)t} + A_2(x,\,t)e^{-i\omega_2(B)t}\end{pmatrix}$$

Assuming the wavepacket reaching the field-zone entrance point $x = 0$ to have the simple pure internal state form: $|\Psi_0(x=0,\,t)\rangle = e^{-\frac{(vt)^2}{\sigma}}\begin{pmatrix}1\\0\end{pmatrix}$, the boundary condition at $x = 0$:

$$|\Psi(x=0,\,t)\rangle = U^\dagger\begin{pmatrix}1 & 0\\ 0 & 1\end{pmatrix}\begin{pmatrix}A_1(0,\,t)e^{-i\omega_1(B)t}\\ A_2(0,\,t)e^{-i\omega_2(B)t}\end{pmatrix} = |\Psi_0(x=0,\,t)\rangle = \exp\left[-\frac{(vt)^2}{\sigma}\right]\begin{pmatrix}1\\0\end{pmatrix}$$

yields for the time-dependent coefficients vector:

$$\begin{pmatrix}a_1(t)\\ a_2(t)\end{pmatrix} = \frac{1}{\sqrt{2}}\begin{pmatrix}e^{ik_1 vt}e^{i\omega_1(B)t}\\ -e^{ik_2 vt}e^{i\omega_2(B)t}\end{pmatrix}$$

The resulting state vector in the field-zone ($0 < x < L$) is therefore:

$$|\Psi(x,\,t)\rangle = \frac{1}{2}e^{-\frac{(x-vt)^2}{\sigma}}\begin{pmatrix}e^{ik_1 x} + e^{ik_2 x}\\ e^{ik_1 x} - e^{ik_2 x}\end{pmatrix}$$

Expanding, up to second order, in the small magnetic-to-kinetic energy ratio $\hbar\gamma B/mv^2$:

$$k_\pm = \frac{1}{\hbar}\sqrt{m^2v^2 \pm m\hbar\gamma B} = k_0\sqrt{1 \pm \frac{\hbar\gamma B}{mv^2}} \approx k_0 \pm \frac{\gamma B}{2v},$$
$$k_0 \equiv \frac{mv}{\hbar}$$

we find:

$$|\Psi(x,\,t)\rangle \simeq e^{-\frac{(x-vt)^2}{\sigma}} e^{ik_0 x} \begin{pmatrix} \cos\left(\frac{1}{2}\gamma B\frac{x}{v}\right) \\ i\sin\left(\frac{1}{2}\gamma B\frac{x}{v}\right) \end{pmatrix},\ 0 \leqslant x \leqslant L \tag{40}$$

Our simplified time-dependent approach, employed in the main text, is obtained from the above fully quantum formulation by treating the spatial coordinate classically at the early stage of the analysis, i.e. by taking $x = vt$ in Eq. (39), which implies: $A_n(x = vt,\, t) = a_n(t)$, so that the boundary condition at $x = 0$ coincides with the initial condition at $t = 0$, or:

$$|\Psi(t=0)\rangle = U^{\dagger}\begin{pmatrix}1\\0\end{pmatrix}A_1 + U^{\dagger}\begin{pmatrix}0\\1\end{pmatrix}A_2 = U^{\dagger}\begin{pmatrix}1 & 0\\ 0 & 1\end{pmatrix}\begin{pmatrix}A_1\\A_2\end{pmatrix} = \begin{pmatrix}1\\0\end{pmatrix} = |\Psi(0)\rangle$$

Solving for the coefficients vector:

$$\begin{pmatrix}A_1\\A_2\end{pmatrix} = \begin{pmatrix}1 & 0\\ 0 & 1\end{pmatrix}U\begin{pmatrix}1\\0\end{pmatrix} = \frac{1}{\sqrt{2}}\begin{pmatrix}1 & 1\\ -1 & 1\end{pmatrix}\begin{pmatrix}1\\0\end{pmatrix} = \frac{1}{\sqrt{2}}\begin{pmatrix}1\\-1\end{pmatrix}$$

the state vector in the time-zone ($\tau > t \geqslant 0$) is:

$$|\Psi(t)\rangle = \frac{1}{\sqrt{2}}\begin{pmatrix}A_1 e^{-i\omega_1(B)t} - A_2 e^{-i\omega_2(B)t}\\ A_1 e^{-i\omega_1(B)t} + A_2 e^{-i\omega_2(B)t}\end{pmatrix} = \begin{pmatrix}\cos\left(\frac{1}{2}\gamma Bt\right)\\ i\sin\left(\frac{1}{2}\gamma Bt\right)\end{pmatrix}$$

which, up to a phase factor, $e^{ik_0 vt} = e^{imv^2 t/\hbar}$, coincides with the full wavepacket approach, Eq. (40), for $x = vt$.

Appendix B

In the quantum description presented in the main text for spin $\frac{1}{2}$ particles it was explained why the detected signal is dominated by the $1/2 \to (1/2)'$ transition. However, the variant of the transition probabilities in some experiments is not so large. In these cases one should take into account matrix elements for all or part of the four pairs of initial and final states

$$|z_{ini}\rangle \leftrightarrow |m_I\rangle \ \text{ and } \ |z_{fin}\rangle \leftrightarrow |m_I'\rangle \tag{41}$$

i.e.:

$$\left\langle (1/2)'\middle|\Psi_2\left(1/2;t=\tfrac{2L}{v}\right)\right\rangle = \cos\left(\tfrac{\Theta_B}{2}\right)\cos[\tau(\gamma/2)(B_1+B_2)] + i\sin\left(\tfrac{\Theta_B}{2}\right)\sin[\tau(\gamma/2)(B_1-B_2)] \tag{42}$$

$$\left\langle (1/2)'\middle|\Psi_2\left(-1/2;t=\tfrac{2L}{v}\right)\right\rangle = -i\cos\left(\tfrac{\Theta_B}{2}\right)\sin[\tau(\gamma/2)(B_1+B_2)] - \sin\left(\tfrac{\Theta_B}{2}\right)\cos[\tau(\gamma/2)(B_1-B_2)] \tag{43}$$

$$\left\langle (-1/2)'\middle|\Psi_2\left(1/2;t=\tfrac{2L}{v}\right)\right\rangle = -i\cos\left(\tfrac{\Theta_B}{2}\right)\sin[\tau(\gamma/2)(B_1+B_2)] + \sin\left(\tfrac{\Theta_B}{2}\right)\cos[\tau(\gamma/2)(B_1-B_2)] \tag{44}$$

$$\left\langle (-1/2)'\middle|\Psi_2\left(-1/2;t=\tfrac{2L}{v}\right)\right\rangle = \cos\left(\tfrac{\Theta_B}{2}\right)\cos[\tau(\gamma/2)(B_1+B_2)] - i\sin\left(\tfrac{\Theta_B}{2}\right)\sin[\tau(\gamma/2)(B_1-B_2)] \tag{45}$$

The corresponding contributions to the spin echo signal:

$$\overline{\left|\left\langle (1/2)'\middle|\Psi_2\left(1/2;t=\tfrac{2L}{v}\right)\right\rangle\right|^2} = \overline{\left|\left\langle (-1/2)'\middle|\Psi_2\left(-1/2;t=\tfrac{2L}{v}\right)\right\rangle\right|^2} =$$
$$= \cos^2\tfrac{\Theta_B}{2}\overline{\cos^2[\tau(\gamma/2)(B_1+B_2)]} + \sin^2\tfrac{\Theta_B}{2}\overline{\sin^2[\tau(\gamma/2)(B_1-B_2)]} \approx$$
$$\approx \cos^2\tfrac{\Theta_B}{2}\left[\tfrac{1}{2} + \tfrac{1}{2}e^{-\left(\frac{\Delta v}{\bar v}\right)^2\left(\frac{\gamma(B_1+B_2)L}{2\bar v}\right)^2}\cos\left(\tfrac{\gamma(B_1+B_2)L}{\bar v}\right)\right] + \sin^2\tfrac{\Theta_B}{2}\left[\tfrac{1}{2} - \tfrac{1}{2}e^{-\left(\frac{\Delta v}{\bar v}\right)^2\left(\frac{\gamma(B_1+B_2)L}{2\bar v}\right)^2}\cos\left(\tfrac{\gamma(B_1-B_2)L}{\bar v}\right)\right] \tag{46}$$

and

$$\overline{\left|\left\langle (1/2)'\middle|\Psi_2\left(-1/2;t=\tfrac{2L}{v}\right)\right\rangle\right|^2} = \overline{\left|\left\langle (-1/2)'\middle|\Psi_2\left(1/2;t=\tfrac{2L}{v}\right)\right\rangle\right|^2} =$$
$$= \cos^2\tfrac{\Theta_B}{2}\overline{\sin^2[\tau(\gamma/2)(B_1+B_2)]} + \sin^2\tfrac{\Theta_B}{2}\overline{\cos^2[\tau(\gamma/2)(B_1-B_2)]} \approx$$
$$\approx \cos^2\tfrac{\Theta_B}{2}\left[\tfrac{1}{2} - \tfrac{1}{2}e^{-\left(\frac{\Delta v}{\bar v}\right)^2\left(\frac{\gamma(B_1+B_2)L}{2\bar v}\right)^2}\cos\left(\tfrac{\gamma(B_1+B_2)L}{\bar v}\right)\right] + \sin^2\tfrac{\Theta_B}{2}\left[\tfrac{1}{2} + \tfrac{1}{2}e^{-\left(\frac{\Delta v}{\bar v}\right)^2\left(\frac{\gamma(B_1+B_2)L}{2\bar v}\right)^2}\cos\left(\tfrac{\gamma(B_1-B_2)L}{\bar v}\right)\right] \tag{47}$$

should be substituted to Eq. (10).

References

[1] Mezei F. Neutron Spin Echo. In: Mezei F, editor. Lect. Notes Phys. vol. 128. Berlin/Heidelberg: Springer; 1980. p. 1–26.
[2] Jardine AP, Alexandrowicz G, Hedgeland H, Allison W, Ellis J. Phys Chem Chem Phys 2009;11:3355.
[3] Jardine AP, Dworski S, Fouquet P, Alexandrowicz G, Riley DJ, Lee GYH, Ellis J, Allison W. Science 2004;304:1790.
[4] Kole PR, Jardine AP, Hedgeland H, Alexandrowicz G. J Phys: Condens Matter 2010;22:304018.
[5] Tamtögl A, Campi D, Bremholm M, Hedegaard EMJ, Iversen BB, Bianchi M, Hofmann P, Marzari N, Benedek G, Ellis J, Allison W. Nanoscale 2018;10:14627.
[6] Godsi O, Corem G, Alkoby Y, Cantin JT, Krems RV, Somers MF, Meyer J, Kroes G-J, Maniv T, Alexandrowicz G. Nat Commun 2017;8:15357.
[7] Lechner BAJ, Hedgeland H, Jardine AP, Allison W, Hinch BJ, Ellis J. Phys Chem Chem Phys 2015;17:21819.
[8] de Haan V-O, Plomp J, van Well AA, Rekveldt MT, Hasegawa YH, Dalgliesh RM, Steinke N-J. Phys Rev A 2014;89:063611.
[9] Fouquet P, Hedgeland H, Jardine A, Alexandrowicz G, Allison W, Ellis J. Physica B 2006;385:269.
[10] Levitt MH. Spin dynamics: basics of nuclear magnetic resonance. Wiley; 2008.
[11] Gähler R, Golub R, Habicht K, Keller T, Felber J. Physica B 1996;229:1.
[12] Golub R, Gahler R. Phys Lett A 1987;123:43.
[13] Häussler W, Schmidt U, Ehlers G, Mezei F. Chem Phys 2003;292:501.
[14] Grigoriev S, Kraan W, Rekveldt M. Phys Rev A 2004;69:043615.
[15] This definition can be generalized for the case that B1 is anti-parallel to the propagation axis X, by deciding that parallel echoes are ones where the polarity of B1 with respect to X is identical to that of B2 with respect to X0, and antiparallel echoes are those where there is a sign difference between the two polarities.
[16] Major J, Farago B, Mezei F. Fernandez-Alonso F, Price DL, editors. Neutron scattering – magnetic and quantum phenomena, experimental methods in the physical sciences, vol. 48. Academic Press; 2015. p. 1–42.
[17] DeKieviet M, Dubbers D, Schmidt C, Scholz D, Spinola U. Phys Rev Lett 1995;75:1919.
[18] Fouquet P, Jardine AP, Dworski S, Alexandrowicz G, Allison W, Ellis J. Rev Sci Inst 2005;76:053109.
[19] Godsi O, Corem G, Kravchuk T, Bertram C, Morgenstern K, Hedgeland H, Jardine AP, Allison W, Ellis J, Alexandrowicz G. J Phys Chem Lett 2015;6:4165.
[20] Tamtögl A, Davey B, Ward DJ, Jardine AP, Ellis J, Allison W. Rev Sci Inst 2018;89:023902.
[21] Alexandrowicz G. Helium spin-echo spectroscopy: measuring the dynamics of atoms, molecules and surfaces (Ph.D. thesis). Cambridge University; 2005.
[22] Y. Alkoby et al. in preparation; 2018.